Nano Research 2017, 10(7): 2482–2494
DOI 10.1007/s12274-017-1452-3
Research Article
ISSN 1998-0124
CN 11-5974/O4

Uniform ordered mesoporous $ZnCo_2O_4$ nanospheres for super-sensitive enzyme-free H_2O_2 biosensing and glucose biofuel cell applications

Shiqiang Cui[1], Li Li[1], Yaping Ding[1] (✉), Jiangjiang Zhang[1], Qingsheng Wu[2], and Zongqian Hu[3] (✉)

[1] *School of Materials Science and Engineering; College of Sciences, Shanghai University, Shanghai 200444, China*
[2] *State Key Laboratory of Pollution Control and Resource Reuse, Tongji University, Shanghai 200444, China*
[3] *Beijing Institute of Radiation Medicine, Beijing 100850, China*

Received: 1 November 2016
Revised: 23 December 2016
Accepted: 1 January 2017

KEYWORDS
mesoporous $ZnCo_2O_4$,
H_2O_2 biosensing,
glucose biofuel cells

ABSTRACT

Uniform, ordered mesoporous $ZnCo_2O_4$ (meso-$ZnCo_2O_4$) nanospheres were successfully synthesized using a sacrificing template method. The meso-$ZnCo_2O_4$ nanospheres were used for the first time for H_2O_2 biosensing and in glucose biofuel cells (GBFCs) as an enzyme mimic. The meso-$ZnCo_2O_4$ nanospheres not only exhibited excellent catalytic performance in the H_2O_2 sensor, achieving a high sensitivity (658.92 $\mu A \cdot mM^{-1} \cdot cm^{-2}$) and low detection limit (0.3 nM at signal-to-noise ratio (S/N) = 3), but also performed as an excellent cathode material in GBFCs, resulting in an open circuit voltage of 0.83 V, maximum power density of 0.32 $mW \cdot cm^{-2}$, and limiting current density of 1.32 $mA \cdot cm^{-2}$. The preeminent catalytic abilities to H_2O_2 and glucose may be associated with the large specific surface area of the mesoporous structure in addition to the intrinsic catalytic activity of $ZnCo_2O_4$. These significant findings provide a successful basis for developing methods for the supersensitive detection of H_2O_2 and enriching catalytic materials for biofuel cells.

1 Introduction

Biosensors and biofuel cells are important research fields. According to the type of electrodes, biosensors and biofuel cells can be classified into two categories, namely, enzyme-based and non-enzyme-based [1, 2]. Previous studies have demonstrated the high activity and excellent selectivity of enzyme-based electrodes; however, the unstable operating environment and fragile stability greatly hinder their practical applications [3]. Non-enzymatic electrodes display excellent characteristics as compared to the enzymatic ones. With the development of nanoscience and nanotechnology, functional nanomaterials serving as enzyme mimics exhibiting satisfactory catalytic properties have been developed. For example, noble metals or noble metal alloys [4], transition-metal oxides [5], composite materials [6, 7], and polymers [8, 9] acting as catalysts have

Address correspondence to Yaping Ding, wdingyp@sina.com; Zongqian Hu, huzongqian@hotmail.com

been reported to exhibit encouraging results. Among these functional nanomaterials, transition-metal oxides play an important role owing to their excellent intrinsic catalytic performance, low cost, and environmental friendly properties.

Currently, mixed transition-metal oxides with a spinel structure are considered as promising catalyst materials, and have attracted increasing attention in the field of electronic materials [10, 11]. For catalytic reactions of H_2O_2 and glucose, mixed transition-metal oxides, such as cobalt-based metal oxides (MCo_2O_4, M = Ni, Mn, Cu, etc), exhibit excellent characteristics, due to the synergistic effects in which the metal oxide with the high oxidation state acts as the oxidizing agent and the other acts as the electron donor with a high conductivity [12–14]. Among cobalt-based metal oxides, $ZnCo_2O_4$ is highly advantageous owing to the presence of zinc ion. Zinc compounds exhibit a relatively satisfactory electronic conductivity, low cost, and environmental friendly properties [15]. Furthermore, zinc has an invariable bivalent state, making it easier to replace the bivalent Co^{2+} ions occupying tetrahedral sites. Thus, the synthesis of $ZnCo_2O_4$ requires a low energy [16]. To date, $ZnCo_2O_4$ nanomaterials with different morphologies including nanoparticles, nanoflakes, nanotubes, and mesoporous microspheres have been fabricated for use in many fields, such as lithium-ion batteries [17–19], supercapacitors [20–22], and gas sensors [23]. However, uniform, ordered meso-$ZnCo_2O_4$ nanospheres serving as catalysts in H_2O_2 sensors and glucose biofuel cells (GBFCs) are not well studied to the best of our knowledge.

As is well known, the catalytic property of a catalyst is not only associated with its intrinsic catalytic capability, but also related to its morphology and structure. Recent theoretical and experimental results revealed that spheroidal nanomaterials exhibit superior catalytic properties [24]. Spherical nanomaterials with a uniform size exhibit improved electrochemical properties [25, 26]. Unlike nanoparticles and nanorods, spheroidal nanomaterials effectively inhibit the occurrence of nanomaterial accumulation on the electrode surface [27, 28]. Moreover, catalytic reactions generally occur on catalyst surfaces and the reaction rate is related to the quantity of molecules reaching the surface, in addition to the intrinsic catalytic properties of the catalyst [29]. Interestingly, mesoporous structures with a high porosity and more available electroactive sites derived from the high specific surface area can effectively accommodate guest molecules, resulting in enhanced catalytic reactions [30, 31].

In this study, uniform, ordered mesoporous $ZnCo_2O_4$ (meso-$ZnCo_2O_4$) nanospheres were successfully synthesized. The meso-$ZnCo_2O_4$ nanomaterials were used as a novel platform for applications in H_2O_2 sensors and GBFCs. The sensor exhibited a high sensitivity (658.92 $\mu A \cdot mM^{-1} \cdot cm^{-2}$), wide linear range (~0.001–900 μM), and low detection limit to H_2O_2 (0.3 nM at a signal-to-noise ratio (S/N) of 3. Furthermore, good response effects were obtained with the GBFCs.

2 Experimental

2.1 Reagents and Apparatus

H_2O_2, glucose, $EO_{20}PO_{70}EO_{20}$ (P123), KOH, NaOH, carbon paper, Pt/C, nafion, N-methylpyrrolidinone (NMP), polyvinylidene fluoride (PVDF), $Zn(NO_3)_2 \cdot 6H_2O$, $Co(NO_3)_2 \cdot 6H_2O$, ascorbic acid (AA), uric acid (UA), tryptophan (Trp), glycocoll (Gly), and dopamine (DA) were purchased from Aladdin Chemical Reagent Co. (Shanghai, China). All chemical reagents were of analytical grade and used directly without further purification. Double-distilled water (18.2 MΩ·cm) was used in all experiments.

Electrochemical measurements, including cyclic voltammetry (CV) and chronoamperometry, were performed on an electrochemical workstation (CHI660D). A traditional three-electrode mode consisting of a meso- or bulk-$ZnCo_2O_4$ modified carbon paste electrode (CPE) acting as the working electrode, saturated calomel reference electrode (SCE), and Pt foil counter electrode was used in 0.3 M NaOH electrolyte with a potential ranging from 0 to 0.65 V for CV and an applied potential of 0.5 V for chronoamperometry measurements. The output current and voltage of the GBFC were monitored using a digital multimeter.

The morphology and structure of the obtained samples were analyzed by employing X-ray diffraction

(XRD; Bruker, D8 Advance diffractometer with Cu-Kα radiation (λ = 1.5418 Å)), X-ray photoelectron spectroscopy (XPS; Thermal ESCALAB 250), transmission electron microscopy (TEM; JEOL JEM-200CX, operating at 160 kV), and field emission scanning electron microscopy (FESEM; JSM-6700F, 15.0 kV). The specific surface area and pore size distribution were examined using nitrogen adsorption–desorption isotherms measured at liquid nitrogen temperature (77 K) using a micrometrics ASAP 2020 sorptometer.

2.2 Preparation of KIT-6 template, meso-$ZnCo_2O_4$, and bulk-$ZnCo_2O_4$ catalysts

The mesoporous KIT-6 hard template was synthesized as described previously [32]. Initially, appropriate amounts of HCl (37%), distilled water, and the surfactant P123 were uniformly mixed. n-Butanol and tetraethyl orthosilicate were then added dropwise to the homogenous aqueous solution under stirring at 35 ℃. Subsequently, the homogeneous solution was autoclaved and heated for 24 h. Finally, the product was filtered, dried in an oven, and calcined in a muffle furnace.

Meso-$ZnCo_2O_4$ nanospheres were prepared using a nanocasting strategy by employing KIT-6 as the template followed by performing calcination [33]. Typically, the KIT-6 template was homogeneously dispersed in 5 mL ethanolic solution containing 2 mM $Co(NO_3)_2{\cdot}6H_2O$ and 1 mM $Zn(NO_3)_2{\cdot}6H_2O$ under continuous stirring for 1 h at 25 ℃. The mixture was then heated at 60 ℃ until ethanol completely evaporated. The sample was then calcined at 200 ℃ for 7 h, and the composite was recasted three times using the same process. The samples were calcined at 450 ℃ for 5 h, and the KIT-6 template was removed using 2 M HF aqueous solution (as shown in the schematic illustration in the Electronic Supplementary Material (ESM)).

For comparison, bulk-$ZnCo_2O_4$ powders were synthesized using a simple two-step route involving sol–gel method and calcination. Initially, $Co(NO_3)_2{\cdot}6H_2O$ (2.34 g) and $Zn(NO_3)_2{\cdot}6H_2O$ (1.19 g) were uniformly dissolved in 60 mL ethanol. The mixture was then heated at 60 ℃ until the solvent completely evaporated under continuous stirring. Finally, the prepared sample was calcined at 450 ℃ for 5 h to obtain the final product.

2.3 Fabrication of meso-$ZnCo_2O_4$/CPE and bulk-$ZnCo_2O_4$/CPE

Before carrying out the modification process, a CPE electrode was fabricated as described previously [34]. Appropriate amounts of meso-$ZnCo_2O_4$ and bulk-$ZnCo_2O_4$ powders were dispersed in 1 mL double-distilled water and ultrasonically agitated for 10 min to obtain a well-dispersed suspension. Finally, 10 μL of the $ZnCo_2O_4$ suspension was dropped on the surface of CPE.

2.4 Fabrication of GBFCs

A fuel cell reactor was fabricated with acrylic glass, and the reactor was divided into anodic and cathodic compartments using an exchange membrane. The output current and voltage were measured using a digital multimeter. The cathode decorated with meso-$ZnCo_2O_4$ or bulk-$ZnCo_2O_4$ was fabricated using the following process: 8 mg $ZnCo_2O_4$ and 2 mg super-p carbon black was uniformly dispersed in 100 mg of the NMP solution containing 1 mg PVDF to form a suspension. Desired amounts of the suspension (5 mg·cm^{-2}) and nafion were uniformly casted onto a carbon paper followed by drying it in air before conducting experiments. Pt/C modified carbon paper acting as the anode was fabricated using the same method. 50 mL of a mixed solution containing 0.1 M glucose and 0.1 M KOH was used as the cathode electrolyte. 50 mL 0.04 M Britton–Robinson buffer (B–R, pH = 2.5) was used as the anode electrolyte. The active area of the electrode was ~ 1 cm × 1 cm. During the reaction, oxygen and nitrogen gases were passed to the anodic and cathodic compartments, respectively, and the reactor was linked with an external resistance.

3 Results and discussion

3.1 Physicochemical properties of meso-$ZnCo_2O_4$

XRD patterns of the as-obtained samples are shown in Fig. 1. The materials exhibited distinct peaks at 2θ = 18.9°, 31.3°, 36.9°, 38.5°, 44.8°, 55.6°, 59.4°, 65.3°, and 72.3°, corresponding to the spinel crystal planes (111), (220), (311), (222), (400), (422), (511), (440), and (620),

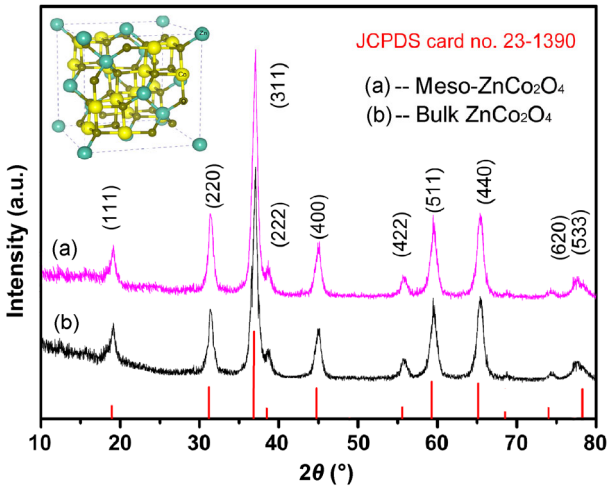

Figure 1 XRD patterns and the crystal structure of $ZnCo_2O_4$.

respectively. No other diffraction peaks were detected. These diffraction peaks can be assigned to the $ZnCo_2O_4$ phase (JCPDS card no. 23-1390), indicating the formation of $ZnCo_2O_4$. The crystal structure of $ZnCo_2O_4$ is displayed in the inset of Fig. 1 [35].

The purity and valence state composition of the meso-$ZnCo_2O_4$ catalysts were investigated using XPS. As shown in Fig. 2(a), the wide-scan spectrum of the as-prepared samples exhibits four elements (Zn, Co, O, and C), corresponding to the chemical composition of meso-$ZnCo_2O_4$. The binding energies of meso-$ZnCo_2O_4$ were corrected by referencing the C 1s peak to 284.5 eV. Figure 2(b) shows the highly distinct Zn 2p spectrum exhibiting two strong peaks at 1,022.5 and 1,045.5 eV, corresponding to Zn $2p_{3/2}$ and Zn $2p_{1/2}$, respectively. This result confirms the presence of Zn (II) oxidation state in $ZnCo_2O_4$ [19, 36]. As shown in Fig. 2(c), two strong peaks are observed in the Co 2p core spectrum at 779.7 and 794.4 eV, corresponding to Co $2p_{3/2}$ and Co $2p_{1/2}$, respectively, confirming the presence of Co (III) oxidation state in $ZnCo_2O_4$ [37]. As displayed in Fig. 2(d), the O 1s region exhibits a doublet at 529.9 and 531.8 eV, which are ascribed to the oxygen species from $ZnCo_2O_4$ and chemisorbed or dissociated oxygen or OH species present on the surface of $ZnCo_2O_4$ nanospheres, respectively [19, 38]. Thus, XPS measurements together with XRD confirm the formation of highly pure $ZnCo_2O_4$.

The morphological features of the as-obtained samples were investigated using SEM and TEM. As shown in Fig. 3(a) and Fig. S1 (in the ESM), meso-$ZnCo_2O_4$

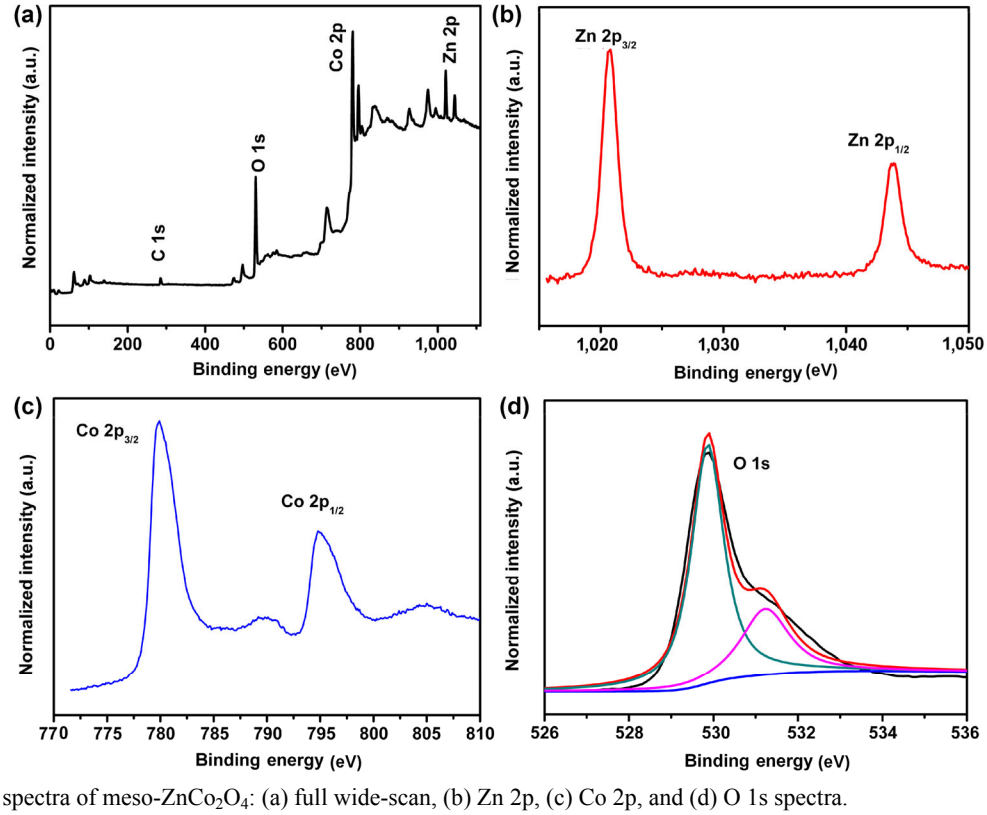

Figure 2 XPS spectra of meso-$ZnCo_2O_4$: (a) full wide-scan, (b) Zn 2p, (c) Co 2p, and (d) O 1s spectra.

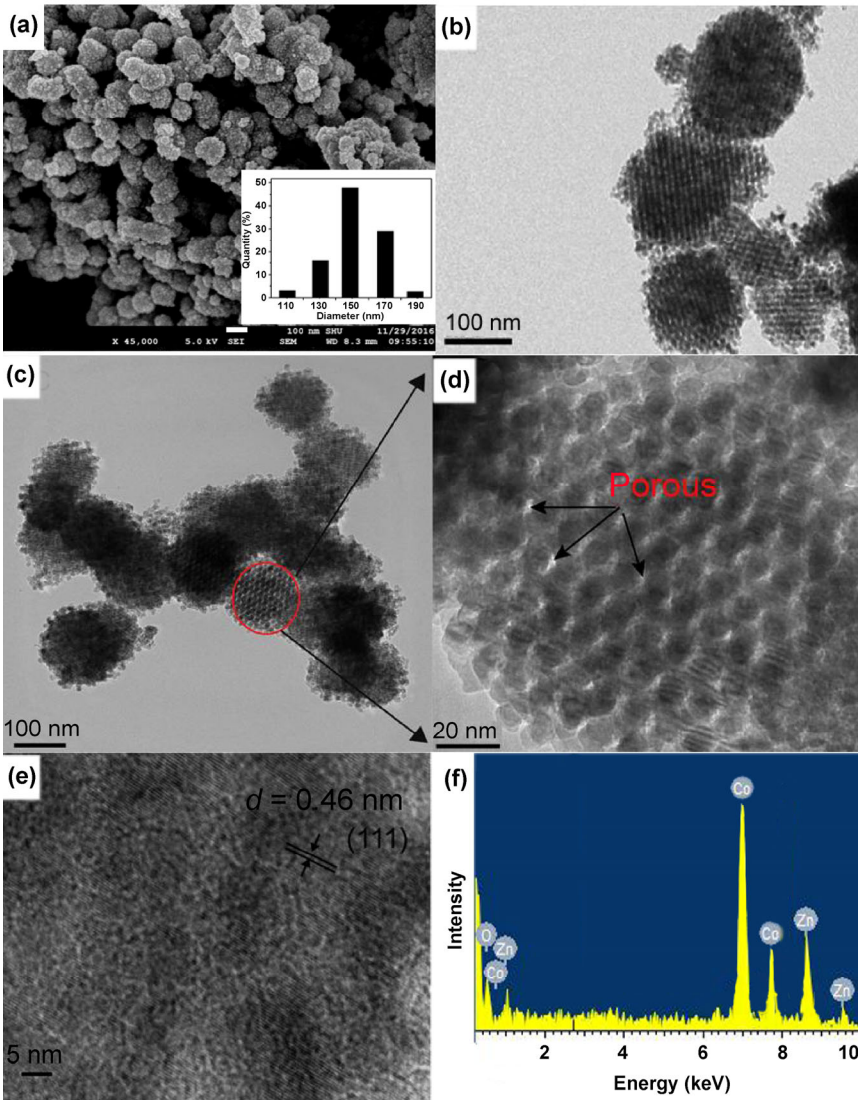

Figure 3 (a) SEM image, (inset of (a)) diameter distribution, (b) TEM image, (c)–(e) HRTEM images, and (f) EDX spectrum of meso-$ZnCo_2O_4$.

exhibits a uniform spheroidal structure with an average diameter of ~150 nm (inset of Fig. 3(a)). However, bulk-$ZnCo_2O_4$ exhibits an irregular morphology. The representative TEM images depicted in Figs. 3(b) and 3(c) indicate that the diameter of the $ZnCo_2O_4$ microspheres is consistent with the SEM results. Each meso-$ZnCo_2O_4$ nanosphere is composed of many well-ordered and highly crystallized $ZnCo_2O_4$ nanoparticles. Figure 3(d) shows the partially enlarged view of meso-$ZnCo_2O_4$. The nanosphere surface is stacked in an orderly fashion with numerous small nanocrystals having a diameter of ~10 nm and forms a conspicuous porous structure with a size of ~3–4 nm (highlighted by arrowheads), which demonstrated the as-obtained samples were geared to mesoporous materials. Such a mesoporous structure exhibits a significantly larger surface area and lower density as compared to the solid counterparts, resulting in the generation of more active sites available for practical catalytic reactions. From Fig. 3(e), the lattice space is measured to be 0.46 nm, corresponding to the theoretical interplanar spacing of spinel $ZnCo_2O_4$ (111) planes. Elemental Co, O, and Zn are present and no extra peaks are detected, in consistent with the XPS results (Fig. 3(f)). Moreover, the atomic ratio of Zn and Co is ~ 1:2, suggesting the formation of $ZnCo_2O_4$.

The specific surface area and pore size distribution of $ZnCo_2O_4$ nanospheres were analyzed by measuring the nitrogen adsorption–desorption isotherm. As shown in Fig. 4, the samples exhibit a type-IV isotherm in the relative pressure range of 0.4–0.9, and the hysteresis loop confirms the existence of the mesoporous structure. In addition, the surface area of meso-$ZnCo_2O_4$ is 106.2 $m^2 \cdot g^{-1}$, which is larger than previously reported values [19, 39]. Most of the pores exhibit a size in the range of ~2–6 nm, and the average pore diameter of meso-$ZnCo_2O_4$ is 3.6 nm as calculated from the adsorption branches of the isotherm by the Barret–Joyner–Halenda (BJH) method. These findings are in consistent with the TEM results. The large surface area of the meso-$ZnCo_2O_4$ causes the availability of more binding sites, thereby enhancing the loading capacities of biological molecules including H_2O_2 and glucose, resulting in an improvement in the oxygen reduction activity.

3.2 Electrochemical behaviors of H_2O_2 on different electrodes

CV was employed to monitor the surface signal change of the modified electrode and evaluate the electrochemical behaviors of different electrodes (containing bare CPE, meso-$ZnCo_2O_4$/CPE and bulk-$ZnCo_2O_4$/CPE) in 0.3 M NaOH electrolyte at a scan rate of 20 $mV \cdot s^{-1}$. Figure 5(a) shows the CV plots of the three electrodes. As compared to the weak redox peaks obtained with bare CPE (curve (1)), a pair of conspicuous redox peaks are obtained at 0.52 V for the anodic peak (E_{pa}) and 0.48 V for the cathodic peak (E_{pc}) with the bulk-$ZnCo_2O_4$/CPE (curve (2)) and meso-$ZnCo_2O_4$/CPE (curve (3)), which could be attributed to the Co(IV)/Co(III) redox couples [40]. The reaction processes can be summarized as follows

$$Co_2O_4^{2-} + 2H_2O \rightleftharpoons 2CoOOH + 2OH^- \quad (1)$$

$$CoOOH + OH^- \rightleftharpoons CoO_2 + H_2O + e^- \quad (2)$$

According to previous reports, a peroxidation process occurs on Co_3O_4 modified electrodes in alkaline solution due to Co (II)/Co (III) redox couples [41, 42]. However, no preoxidation peak is observed with the $ZnCo_2O_4$ modified electrode during the catalytic process. This is because the tetrahedral sites of Co_3O_4 are occupied by zinc ions, resulting in the absence of Co (II), and Co (III) acts as the predominant ion in the electrocatalytic process due to the occurrence of Co (IV)/Co (III) redox reaction Additionally, the enclosed areas of the CV loops obtained with the bulk-$ZnCo_2O_4$/CPE (curve (2)) and meso-$ZnCo_2O_4$/CPE (curve (3)) are larger than that of the bare CPE, indicating the excellent capacitance of $ZnCo_2O_4$. The meso-$ZnCo_2O_4$/CPE (curve (3)) exhibits a larger enclosed area than the bulk-$ZnCo_2O_4$/CPE (curve (2)), suggesting the higher chemical reactivity of meso-$ZnCo_2O_4$ as compared to bulk-$ZnCo_2O_4$ [43], which could be associated to the large surface area of the mesoporous structure.

Figure 5(b) illustrates the electrocatalytic capabilities of meso-$ZnCo_2O_4$/CPE and bulk-$ZnCo_2O_4$/CPE in 0.3 M NaOH electrolyte with different concentrations of H_2O_2. The oxidation peak current (I_{pa}) of H_2O_2 remarkably increases in the case of meso-$ZnCo_2O_4$/CPE and bulk-$ZnCo_2O_4$/CPE on introducing H_2O_2 and increasing the concentration of H_2O_2 from 0.4 to 1.2 mM. Compared to that of meso-$ZnCo_2O_4$/CPE and bulk-$ZnCo_2O_4$/CPE, weaker redox signals are detected with the bare CPE (Fig. S2 in the ESM). Furthermore, the current response is higher with the meso-$ZnCo_2O_4$/CPE than that with the bulk-$ZnCo_2O_4$/CPE (inset of the Fig. 5(b)). This phenomenon not only demonstrates the excellent catalytic capability of $ZnCo_2O_4$ to H_2O_2, but also reveals the higher peak current density of the mesoporous structure as compared to the bulk one. In contrast, the cathode current

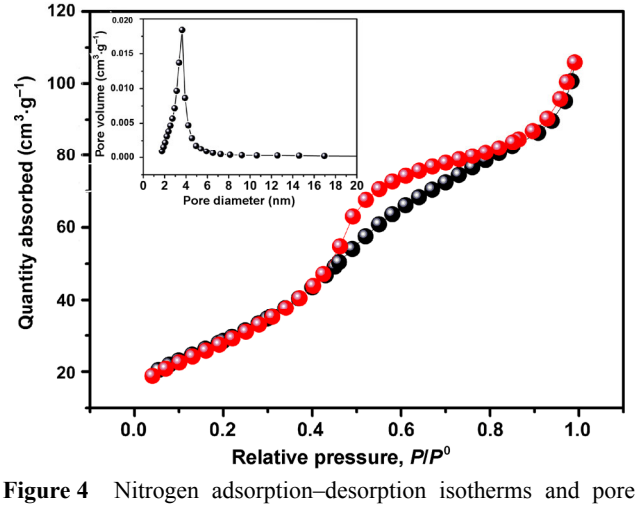

Figure 4 Nitrogen adsorption–desorption isotherms and pore size distribution of meso-$ZnCo_2O_4$.

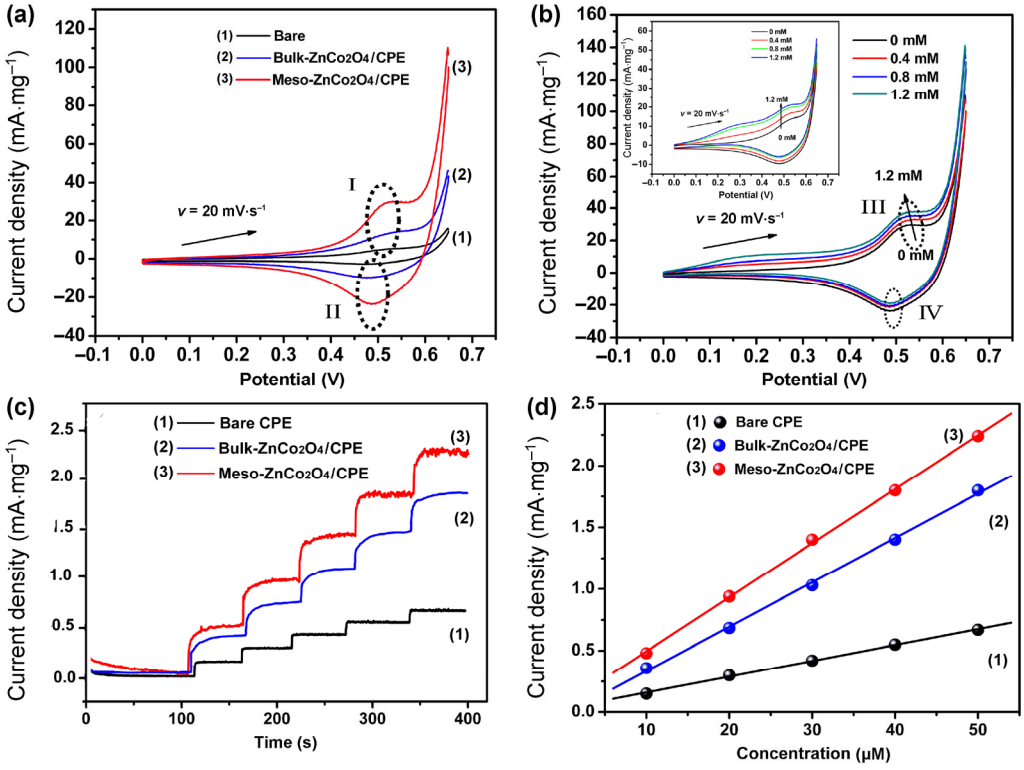

Figure 5 (a) CV plots obtained with the bare CPE (curve (1)), bulk $ZnCo_2O_4$/CPE (curve (2)), and meso-$ZnCo_2O_4$/CPE (curve (3)) in 0.3 M NaOH at 20 mV·s^{-1}. (b) CV plots obtained with the meso-$ZnCo_2O_4$/CPE in 0.3 M NaOH electrolyte with different H_2O_2 concentrations (from 0 to 1.2 mM) at 20 mV·s^{-1}. (c) Amperometric responses of H_2O_2 measured with the bare CPE (curve (1)), bulk $ZnCo_2O_4$/CPE (curve (2)), and meso-$ZnCo_2O_4$/CPE (curve (3)) under the successive injection of H_2O_2 (from 10 to 50 μM). (d) Plot of response current of H_2O_2 versus the corresponding H_2O_2 concentration (μM).

(I_{pc} labeled IV) exhibits inconspicuous changes with an increase in H_2O_2 concentration, exhibiting lower values than that of the blank solution. These findings may be associated to the following reasons. In the absence of H_2O_2, E_{pa} (labeled I) is attributed to the Co(III)/Co(IV) redox couple (Eq. (2)). In this process, Co(III) is oxidized to form Co(IV), resulting in an increase in electrochemical signal. According to previous reports [44], the electrochemical oxidation of H_2O_2 on Co-based materials (labeled III) could be associated to the Co(III)/Co(II) (Eq. (3)) redox couple in basic solution. In other words, Co(III) is easily reduced to form Co(II) by H_2O_2 in alkaline solution, and CoO_2 is not produced. Therefore, it can be speculated that I_{pc} (labeled IV) is caused by $Co(OH)_2$. Co(II) is not dominant in the electrochemical catalysis of H_2O_2, leading to a decrease in I_{pc} as compared to that of the blank solution (labeled II and IV) caused by the Co(IV)/Co(III) redox couple.

$$2CoOOH + H_2O_2 + 2OH^- \rightarrow 2Co(OH)_2 + O_2 + 2H_2O + 2e^- \quad (3)$$

In order to explore the electrochemical response of H_2O_2 on different electrodes, chronoamperometry was employed at an applied potential of +0.5 V with the successive injection of H_2O_2 into 0.3 M NaOH electrolyte under stirring. As shown in Fig. 5(c), meso-$ZnCo_2O_4$/CPE (curve (3)) exhibits a larger response current as compared to the other samples (curves (1) and (2)). Calibration curves were obtained with steady current-time response (Fig. 5(d)). The slope of the calibration curve reflects the sensitivity of the material. Therefore, a higher sensitivity to H_2O_2 is achieved with the meso-$ZnCo_2O_4$/CPE (curve (3), 628.57 μA·mM^{-1}·cm^{-2}) than that with the bare CPE (curve (1), 175.71 μA·mM^{-1}·cm^{-2}) and bulk-$ZnCo_2O_4$/CPE (curve (2), 482.14 μA·mM^{-1}·cm^{-2}). These findings reconfirm the superior electrochemical reaction

occurring on the meso-$ZnCo_2O_4$/CPE. The chronoamperometry results are in good agreement with the CV results. The stronger response current achieved with the meso-$ZnCo_2O_4$/CPE could be attributed to the large specific surface area of meso-$ZnCo_2O_4$, which provides more active sites for the electrochemical oxidation of H_2O_2. Thus, meso-$ZnCo_2O_4$/CPE exhibits higher electro-catalytic capability to H_2O_2 as compared to the bulk counterparts. Hence, it is promising to be used as a novel sensor for electrochemical detection of H_2O_2.

3.3 Effect of operational parameters

The electrochemical kinetics of the meso-$ZnCo_2O_4$/CPE was examined in 0.3 M NaOH electrolyte containing 100 μM H_2O_2 by CV in the potential range of 0–0.65 V with different scan rates. As shown in Fig. 6(a), a continued expansion of the CV background and sustained increase of oxidation peak currents (I_{pa}) together with relatively stable redox peaks potentials are achieved with meso-$ZnCo_2O_4$/CPE on increasing the scan rate from 10 to 200 mV·s^{-1}, indicating the steady electrochemical capability of meso-$ZnCo_2O_4$. I_{pa} and I_{pc} linearly increase with an increase in the scan rate (Fig. 6(b)), and the regression equations can be expressed as

I_{pa} (μA) = 6.9 + 0.41v (mV·s^{-1}) (R = 0.996) and I_{pc} (μA) = –3.7 – 0.14v (mV·s^{-1}) (R = 0.996), respectively, indicating the electrochemical process to be a surface-controlled process.

In order to improve the electrochemical response signal of the H_2O_2 sensor, three major factors, namely, the concentration of NaOH electrolyte, applied potential, and concentration of meso-$ZnCo_2O_4$ were optimized to be 0.3 M, +0.5 V, and 1.0 mg·mL^{-1}, respectively (Fig. S3 in the ESM).

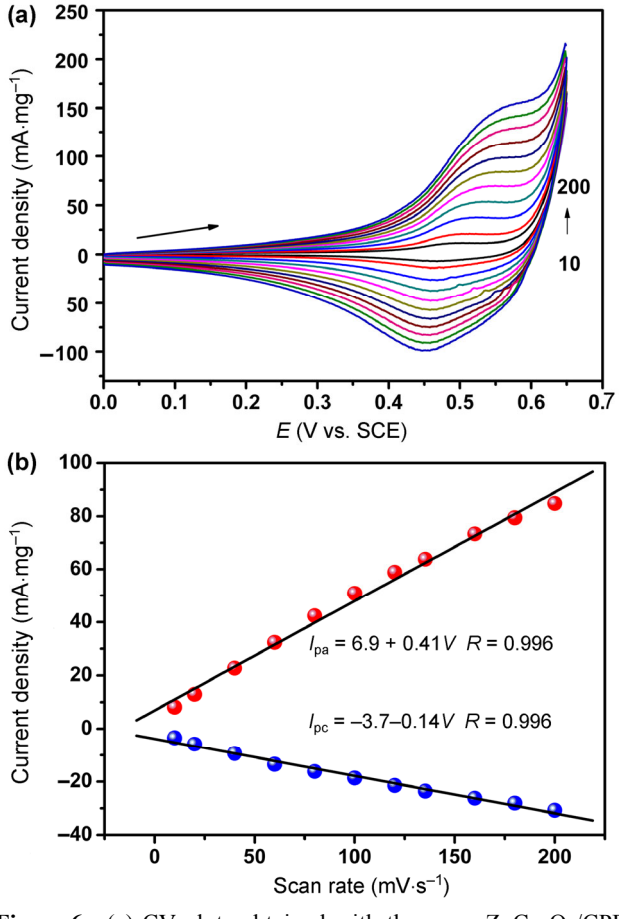

Figure 6 (a) CV plots obtained with the meso-$ZnCo_2O_4$/CPE in 0.3 M NaOH electrolyte at different scan rates (from 10 to 200 mV·s^{-1}). (b) Peak currents versus the scan rate.

3.4 Amperometric detection of H_2O_2

Under optimal conditions, the electrochemical detection of H_2O_2 with the meso-$ZnCo_2O_4$/CPE was examined by employing chronoamperometry. A steady-state current (95%) is achieved within 5.2 s of injecting H_2O_2, revealing the quick recovery capability of meso-$ZnCo_2O_4$ (inset (1) in Fig. 7(a)). The quick recovery phenomenon is likely attributed to the excellent electron/mass transfer occurring in $ZnCo_2O_4$ and large specific surface area of the mesoporous structure. As displayed in Figs. 7(a) and 7(b), I_{pa} linearly increases on changing the H_2O_2 concentration from 0.001 to 900 μM, and the linear regression equation is given as follows: I_{pa} (μA) = 0.046 + 0.046c (μM) (R = 0.998). The detection limit and sensitivity to H_2O_2 are 0.3 nM (S/N = 3) and 658.92 μA·mM^{-1}·cm^{-2}, respectively. As compared to previous reports (shown in Table 1), the proposed sensor exhibits excellent characteristics including a lower detection limit, higher sensitivity, and wider linear range. The excellent intrinsic catalytic properties of $ZnCo_2O_4$ and large specific surface area of the mesoporous structure could be the main reasons for obtaining enhanced catalytic effects for H_2O_2.

3.5 Reproducibility, stability, and selectivity

The reproducibility of the electrode was investigated under optimal conditions to compare the amperometric

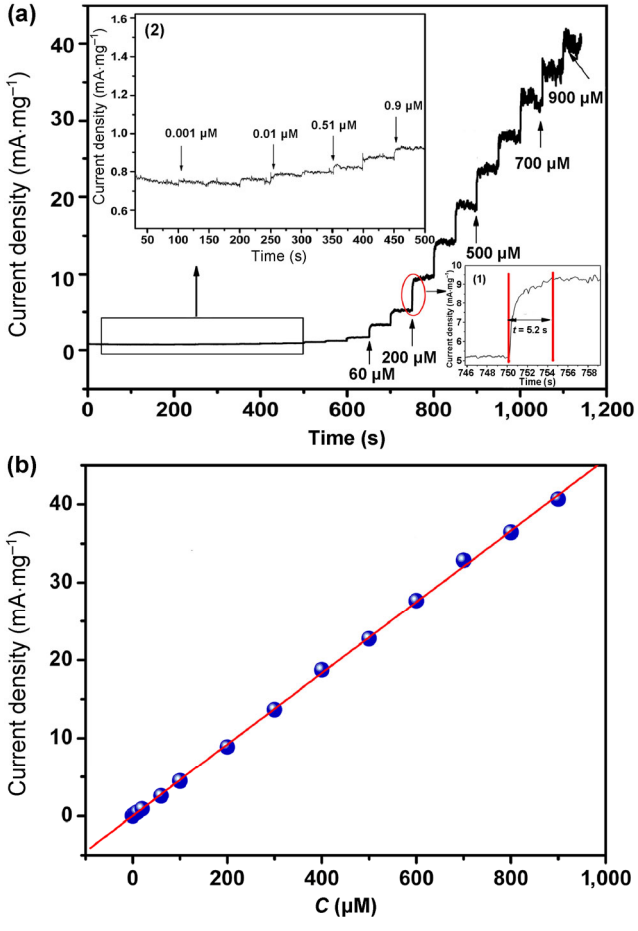

Figure 7 (a) Current–time curve obtained at different H_2O_2 concentrations with meso-$ZnCo_2O_4$/CPE in 0.3 M NaOH electrolyte at +0.5 V. Insets (1) and (2) show the response time with H_2O_2 addition and current–time curve for H_2O_2 at a low concentration. (b) Calibration curve for H_2O_2 on meso-$ZnCo_2O_4$/CPE.

Table 1 Comparison of meso-$ZnCo_2O_4$/CPE and other electrodes

Electrode	Linear range (μM)	Detection limit (μM)	Reference
1D Co_3O_4	15–675	2.4	[45]
Pt-pC_xN_{1-x}	25–572.5	2.29	[46]
Meso-Sm_2O_3	1–320	1	[47]
Ag NPs/porous silicon	1.65–500	0.45	[48]
Ag/C	0.1–500	0.1	[49]
Au/r-GO/TNTs	0.01–22.3	0.006	[50]
F1-CFP	50–500	18	[51]
Meso-$ZnCo_2O_4$	0.001–900	0.0003	This work

responses of faradic currents of 50 μM H_2O_2 by conducting six sets of parallel experiments in 0.3 M NaOH electrolyte. The electrodes were prepared in accordance with the details given in section 2.3. After performing six independent experiments, the relative standard deviation (% RSD) was calculated to be 4.06%, corresponding to the faradic current of H_2O_2 (Fig. S4(a) in the ESM). The stability was also investigated by a commonly used method where the modified electrode was maintained at 4 °C for one week and H_2O_2 was detected each day. Amperometric responses to H_2O_2, similar to the initial value were obtained (Fig. S4(b) in the ESM). Thus, the sensor exhibits excellent reproducibility and stability.

The possible influence factors were investigated to evaluate the anti-interference ability. The detection of H_2O_2 (40 μM) was studied by adding 5 μM DA, UA, Trp, and AA (Fig. S5 in the ESM). Obvious signal changes could not be observed, indicating the good anti-interference ability of meso-$ZnCo_2O_4$/CPE.

3.6 Electrochemical behaviors of glucose on different electrodes and fabrication of non-enzymatic biofuel cells

Electrochemical behaviors of the modified electrodes in the electrocatalysis of glucose were examined using the same method mentioned in section 3.2. The CV responses of 200 μM glucose were investigated with the bare CPE, bulk-$ZnCo_2O_4$/CPE, and meso-$ZnCo_2O_4$/CPE in 0.1 M KOH at a scan rate of 20 $mV \cdot s^{-1}$ (Fig. 8(a)). An extremely weak and negligible redox reaction is achieved with the bare CPE (inset of Fig. 8(a)). In contrast, in the presence of 200 μM glucose, an obvious glucose oxidation peak is obtained at 0.55 V with the meso-$ZnCo_2O_4$/CPE and bulk-$ZnCo_2O_4$/CPE (curves (2) and (4)) as compared to the blank solution (curves (1) and (3)), which is attributed to the Co(IV)/Co(III) redox couple [52]. Moreover, a larger oxidation current is detected with the meso-$ZnCo_2O_4$/CPE than that with bulk-$ZnCo_2O_4$/CPE, which could be attributed to the mesoporous structure. Figure 8(b) shows the time current curves of glucose oxidation at an applied potential of +0.55 V in 0.1 M KOH electrolyte with the persistent injection of glucose under stirring. As similar to the CV plot of bare CPE, an extremely weak response current is obtained with the bare CPE (curve (1)) as compared to the meso-$ZnCo_2O_4$/CPE (curve (3)) and bulk-$ZnCo_2O_4$/CPE (curve (2)). However,

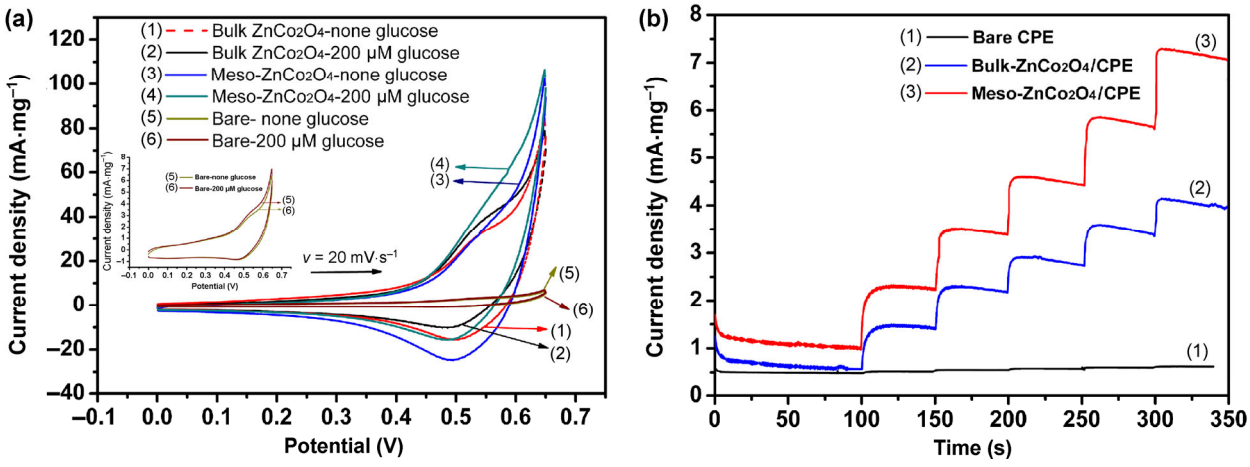

Figure 8 (a) CV plots in the absence (curves (1), (3), and (5)) and presence (curves (2), (4), and (6)) of 200 μM glucose on bare CPE, bulk-$ZnCo_2O_4$/CPE and meso-$ZnCo_2O_4$/CPE in 0.1 M KOH at a scan of 20 mV·s^{-1}. Inset shows the enlarged view of the curves (5) and (6). (b) Amperometric responses of glucose on bare CPE (curve (1)), bulk-$ZnCo_2O_4$/CPE (curve (2)), and meso-$ZnCo_2O_4$/CPE (curve (3)) under the successive injection of 10 to 50 μM glucose.

a higher and stronger response current (curve (3)) is generated with the meso-$ZnCo_2O_4$/CPE than that with the bulk-$ZnCo_2O_4$/CPE (curve (2)). These results demonstrate the excellent catalytic capability of meso-$ZnCo_2O_4$ to glucose.

The meso-$ZnCo_2O_4$ nanospheres exhibit excellent catalytic activity to glucose, offering scientific foundation for the design of GBFC as a cathode modification material. Hence, we fabricated an H-type GBFC (named GBFC I) using meso-$ZnCo_2O_4$ nanomaterial modified carbon paper as cathode and commercial Pt/C modified carbon paper as the anode. For comparison, another GBFC (named GBFC II) was designed using the same method by replacing meso-$ZnCo_2O_4$ with bulk-$ZnCo_2O_4$.

The polarization and power density curves obtained on the two GBFCs are shown in Fig. 9, and the relevant results are summarized in Table 2. The slope of the linear region of the polarization curve derived from GBFC II (line (a)) is higher than that of GBFC I (line (b)), indicating the lower internal resistance of GBFC I [53]. Moreover, the cell performance of GBFC I is superior to that of GBFC II. These findings reveal that meso-$ZnCo_2O_4$ exhibit enhanced catalytic properties toward glucose, in good agreement with the CV results shown in Fig. 8. Hence, meso-$ZnCo_2O_4$ with a large specific surface area is a promising cathode material in GBFCs.

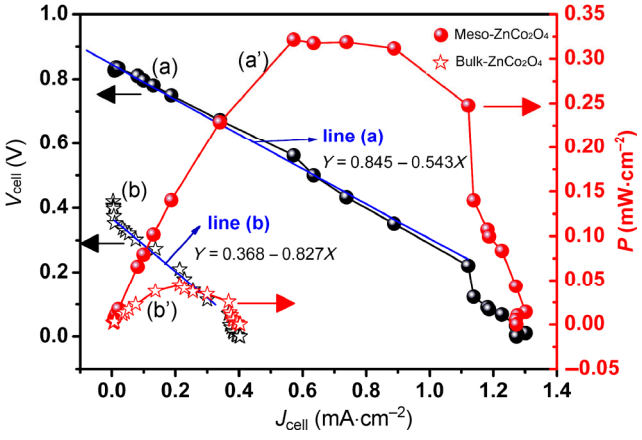

Figure 9 Polarization curves (a) and (b) and power output curves (a') and (b') of the GBFCs. Experimental conditions: a solution containing 0.1 M H_2O_2 and 0.1 M KOH as the cathode electrolyte and 0.04 M B–R solution (pH = 2.5) as the anode electrolyte.

Table 2 Data obtained with GBFC I and GBFC II

GBFC	Open circuit voltage (V)	Maximum power density (mW·cm^{-2})	Limiting current density (mA·cm^{-2})
GBFC I	0.83	0.32	1.32
GBFC II	0.42	0.04	0.41

4 Conclusions

In conclusion, uniform, ordered meso-$ZnCo_2O_4$ nanospheres were successfully prepared using a nanocasting

method followed by employing calcination. Meso-$ZnCo_2O_4$ exhibits an excellent electrocatalytic response to H_2O_2 with a quick response time (5.2 s), high sensitivity (658.92 $\mu A \cdot mM^{-1} \cdot cm^{-2}$), low detection limit (0.3 nM), and wide linear range (~0.001–900 μM). Meso-$ZnCo_2O_4$ exhibits excellent catalytic performance to glucose as a cathode material in GBFCs, with an open circuit voltage of 0.83 V, maximum power density of 0.32 $mW \cdot cm^{-2}$, and limiting current density of 1.32 $mA \cdot cm^{-2}$. The present study not only explores the fabrication of a super-sensitive novel non-enzymatic H_2O_2 sensor but also demonstrates methods for the development of fuel cells. We expect that meso-$ZnCo_2O_4$ nanospheres could be used in more fields in future.

Acknowledgements

Thank the National Natural Science Foundation of China (Nos. 21671132 and 81301345) for the supports. Thank Analysis and Determination Center, Shanghai University for the support.

Electronic Supplementary Material: Supplementary material (XRD pattern, XPS spectra, electrochemial performances of MnO_2 and Fe_2O_3, CV curves of M-MSCs and F-MSCs, the thicknesses of MnO_2 and Fe_2O_3 microelectrodes, stack capacitances curves, and Ragone plot of A-MSCs, M-MSCs and F-MSCs) is available in the online version of this article at http://dx.doi.org/10.1007/s12274-017-1452-3.

References

[1] Yao, S. J.; Guvench, S.; Guvench, M. G.; Kuller, A. E.; Chan, L. T.; Wolfson, S. K., Jr. Glucose sensing in the low and negative region: Utilization of a thin-film electrode. *J. Electroanal. Chem. Interfacial Electrochem.* **1991**, *321*, 211–222.

[2] Stahl, S. S. Palladium-catalyzed oxidation of organic chemicals with O_2. *Science* **2005**, *309*, 1824–1826.

[3] Yuhashi, N.; Tomiyama, M.; Okuda, J.; Igarashi, S.; Ikebukuro, K.; Sode, K. Development of a novel glucose enzyme fuel cell system employing protein engineered PQQ glucose dehydrogenase. *Biosens. Bioelectron.* **2005**, *20*, 2145–2150.

[4] Gu, J.; Zhang, Y. W.; Tao, F. Shape control of bimetallic nanocatalysts through well-designed colloidal chemistry approaches. *Chem. Soc. Rev.* **2012**, *41*, 8050–8065.

[5] Zhang, E. H.; Yu, X.; Ci, S. Q.; Jia, J. C.; Wen, Z. H. Porous Co_3O_4 hollow nanododecahedra for nonenzymatic glucose biosensor and biofuel cell. *Biosens. Bioelectron.* **2016**, *81*, 46–53.

[6] Ci, S. Q.; Wen, Z. H.; Mao, S.; Hou, Y.; Cui, S. M.; He, Z.; Chen, J. H. One-pot synthesis of high-performance Co/graphene electrocatalysts for glucose fuel cells free of enzymes and precious metals. *Chem. Commun.* **2015**, *51*, 9354–9357.

[7] Liu, M. M.; Liu, R.; Chen, W. Graphene wrapped Cu_2O nanocubes: Non-enzymatic electrochemical sensors for the detection of glucose and hydrogen peroxide with enhanced stability. *Biosens. Bioelectron*. **2013**, *45*, 206–212.

[8] Hua, M. Y.; Chen, H. C.; Tsai, R. Y.; Leu, Y. L.; Liu, Y. C.; Lai, J. T. Synthesis and characterization of carboxylated polybenzimidazole and its use as a highly sensitive and selective enzyme-free H_2O_2 sensor. *J. Mater. Chem.* **2011**, *21*, 7254–7262.

[9] Kuwahara, T.; Ohta, H.; Kondo, M.; Shimomura, M. Immobilization of glucose oxidase on carbon paper electrodes modified with conducting polymer and its application to a glucose fuel cell. *Bioelectrochemistry* **2008**, *74*, 66–72.

[10] Hu, L. H.; Peng, Q.; Li, Y. D. Selective synthesis of Co_3O_4 nanocrystal with different shape and crystal plane effect on catalytic property for methane combustion. *J. Am. Chem. Soc.* **2008**, *130*, 16136–16137.

[11] Xiao, X. L.; Liu, X. F.; Zhao, H.; Chen, D. F.; Liu, F. Z.; Xiang, J. H.; Hu, Z. B.; Li, Y. D. Facile shape control of Co_3O_4 and the effect of the crystal plane on electrochemical performance. *Adv. Mater.* **2012**, *24*, 5762–5766.

[12] Kuo, C. C.; Lan, W. J.; Chen, C. H. Redox preparation of mixed-valence cobalt manganese oxide nanostructured materials: Highly efficient noble metal-free electrocatalysts for sensing hydrogen peroxide. *Nanoscale* **2014**, *6*, 334–341.

[13] Wu, M. Y.; Meng, S. J.; Wu, Q.; Si, W. L.; Huang, W.; Dong, X. C. Nickel–cobalt oxide decorated three-dimensional graphene as an enzyme mimic for glucose and calcium detection. *ACS Appl. Mater. Interfaces* **2015**, *7*, 21089–21094.

[14] Sun, C. C.; Yang, J.; Dai, Z. Y.; Wang, X. W.; Zhang, Y. F.; Li, L. Q.; Chen, P.; Huang, W.; Dong, X. C. Nanowires assembled from $MnCo_2O_4$@C nanoparticles for water splitting and all-solid-state supercapacitor. *Nano Res.* **2016**, *9*, 1300–1309.

[15] Guan, B. K.; Guo, D.; Hu, L. L.; Zhang, G. H.; Fu, T.; Ren, W. J.; Li, J. D.; Li, Q. H. Facile synthesis of $ZnCo_2O_4$ nanowire cluster arrays on Ni foam for high-performance asymmetric supercapacitors. *J. Mater. Chem. A* **2014**, *2*, 16116–16123.

[16] Zhao, R. Z.; Li, Q.; Wang, C. X.; Yin, L. W. Highly ordered mesoporous spinel $ZnCo_2O_4$ as a high-performance anode material for lithium-ion batteries. *Electrochim. Acta* **2016**, *197*, 58–67.

[17] Sharma, Y.; Sharma, N.; Subba Rao, G. V.; Chowdari, B. V. R. Nanophase $ZnCo_2O_4$ as a high performance anode material for Li-ion batteries. *Adv. Funct. Mater.* **2007**, *17*, 2855–2861.

[18] Luo, W.; Hu, X. L.; Sun, Y. M.; Huang, Y. H. Electrospun porous $ZnCo_2O_4$ nanotubes as a high-performance anode material for lithium-ion batteries. *J. Mater. Chem.* **2012**, *22*, 8916–8921.

[19] Hu, L. L.; Qu, B. H.; Li, C. C.; Chen, Y. J.; Mei, L.; Lei, D. N.; Chen, L. B.; Li, Q. H.; Wang, T. H. Facile synthesis of uniform mesoporous $ZnCo_2O_4$ microspheres as a high-performance anode material for Li-ion batteries. *J. Mater. Chem. A* **2013**, *1*, 5596–5602.

[20] Liu, B.; Liu, B. Y.; Wang, Q. F.; Wang, X. F.; Xiang, Q. Y.; Chen, D.; Shen, G. Z. New energy storage option: Toward $ZnCo_2O_4$ nanorods/nickel foam architectures for high-performance supercapacitors. *ACS Appl. Mater. Interfaces* **2013**, *5*, 10011–10017.

[21] Zhou, G.; Zhu, J.; Chen, Y. J.; Mei, L.; Duan, X. C.; Zhang, G. H.; Chen, L. B.; Wang, T. H.; Lu, B. G. Simple method for the preparation of highly porous $ZnCo_2O_4$ nanotubes with enhanced electrochemical property for supercapacitor. *Electrochim. Acta* **2014**, *123*, 450–455.

[22] Cheng, J. B.; Lu, Y.; Qiu, K. W.; Yan, H. L.; Hou, X. Y.; Xu, J. Y.; Han, L.; Liu, X. M.; Kim, J.-K.; Luo, Y. S. Mesoporous $ZnCo_2O_4$ nanoflakes grown on nickel foam as electrodes for high performance supercapacitors. *Phys. Chem. Chem. Phys.* **2015**, *17*, 17016–17022.

[23] Park, H. J.; Kim, J.; Choi, N.-J.; Song, H.; Lee, D.-S. Nonstoichiometric Co-rich $ZnCo_2O_4$ hollow nanospheres for high performance formaldehyde detection at ppb levels. *ACS Appl. Mater. Interfaces* **2016**, *8*, 3233–3240.

[24] Anu Prathap, M. U.; Wei, C.; Sun, S. G.; Xu, Z. J. A new insight into electrochemical detection of eugenol by hierarchical sheaf-like mesoporous $NiCo_2O_4$. *Nano Res.* **2015**, *8*, 2636–2645.

[25] Zhu, M. Y.; Meng, D. H.; Wang, C. J.; Diao, G. W. Facile fabrication of hierarchically porous $CuFe_2O_4$ nanospheres with enhanced capacitance property. *ACS Appl. Mater. Interfaces* **2013**, *5*, 6030–6037.

[26] Li, J. F.; Xiong, S. L.; Liu, Y. R.; Ju, Z. C.; Qian, Y. T. High electrochemical performance of monodisperse $NiCo_2O_4$ mesoporous microspheres as an anode material for Li-ion batteries. *ACS Appl. Mater. Interfaces* **2013**, *5*, 981–988.

[27] Zhang, Z.; Liu, X. Q.; Wu, Y.; Zhao, H. Y. Graphene modified Li_2FeSiO_4/C composite as a high performance cathode material for lithium-ion batteries. *J. Solid State Electrochem.* **2015**, *19*, 469–475.

[28] Shen, M. J.; Zhang, Z.; Ding, Y. P. Synthesizing NiAl-layered double hydroxide microspheres with hierarchical structure and electrochemical detection of hydroquinone and catechol. *Microchem. J.* **2016**, *124*, 209–214.

[29] He, C.; Liu, X. H.; Shi, J. W.; Ma, C. Y.; Pan, H.; Li, G. L. Anionic starch-induced Cu-based composite with flake-like mesostructure for gas-phase propanal efficient removal. *J. Colloid Interface Sci.* **2015**, *454*, 216–225.

[30] Deng, W. F.; Yuan, X. Y.; Tan, Y. M.; Ma, M.; Xie, Q. J. Three-dimensional graphene-like carbon frameworks as a new electrode material for electrochemical determination of small biomolecules. *Biosens. Bioelectron.* **2016**, *85*, 618–624.

[31] Wang, D. S.; Zhao, P.; Li, Y. D. General preparation for Pt-based alloy nanoporous nanoparticles as potential nanocatalysts. *Sci. Rep.* **2011**, *1*, 37.

[32] Kleitz, F.; Choi, S. H.; Ryoo, R. Cubic *Ia3d* large mesoporous silica: Synthesis and replication to platinum nanowires, carbon nanorods and carbon nanotubes. *Chem. Commun.* **2003**, 2136–2137.

[33] Wang, Y. Q.; Yang, C. M.; Schmidt, W.; Spliethoff, B.; Bill, E.; Schüth, F. Weakly ferromagnetic ordered mesoporous Co_3O_4 synthesized by nanocasting from vinyl-functionalized cubic *Ia3d* mesoporous silica. *Adv. Mater.* **2005**, *17*, 53–56.

[34] Xu, D.; Luo, L. Q.; Ding, Y. P.; Jiang, L.; Zhang, Y. T.; Ouyang, X. Q.; Liu, B. D. A novel nonenzymatic fructose sensor based on electrospun $LaMnO_3$ fibers. *J. Electroanal. Chem.* **2014**, *727*, 21–26.

[35] Wu, C.; Cai, J. J.; Zhang, Q. B.; Zhou, X.; Zhu, Y.; Li, L. J.; Shen, P. K.; Zhang, K. L. Direct growth of urchin-like $ZnCo_2O_4$ microspheres assembled from nanowires on nickel foam as high-performance electrodes for supercapacitors. *Electrochim. Acta* **2015**, *169*, 202–209.

[36] Vijayanand, S.; Joy, P. A.; Potdar, H. S.; Patil, D.; Patil, P. Nanostructured spinel $ZnCo_2O_4$ for the detection of LPG. *Sens. Actuators B: Chem.* **2011**, *152*, 121–129.

[37] Varghese, B.; Teo, C. H.; Zhu, Y. W.; Reddy, M. V.; Chowdari, B. V. R.; Wee, A. T. S.; Tan, V. B. C.; Lim, C. T.; Sow, C. H. Co_3O_4 nanostructures with different morphologies and their field-emission properties. *Adv. Funct. Mater.* **2007**, *17*, 1932–1939.

[38] Xu, J. B.; Gao, P.; Zhao, T. S. Non-precious Co_3O_4 nano-rod electrocatalyst for oxygen reduction reaction in anion-exchange membrane fuel cells. *Energy Environ. Sci.* **2012**, *5*, 5333–5339.

[39] Bai, J.; Li, X. G.; Liu, G. Z.; Qian, Y. T.; Xiong, S. L. Unusual formation of $ZnCo_2O_4$ 3D hierarchical twin

microspheres as a high-rate and ultralong-life lithium-ion battery anode material. *Adv. Funct. Mater.* **2014**, *24*, 3012–3020.

[40] Tan, Y.; Wu, C. C.; Lin, H.; Li, J. B.; Chi, B.; Pu, J.; Jian, L. Insight the effect of surface Co cations on the electrocatalytic oxygen evolution properties of cobaltite spinels. *Electrochim. Acta* **2014**, *121*, 183–187.

[41] Koza, J. A.; He, Z.; Miller, A. S.; Switzer, J. A. Electrodeposition of crystalline Co_3O_4—A catalyst for the oxygen evolution reaction. *Chem. Mater.* **2012**, *24*, 3567–3573.

[42] Chou, N. H.; Ross, P. N.; Bell, A. T.; Tilley, T. D. Comparison of cobalt-based nanoparticles as electrocatalysts for water oxidation. *ChemSusChem* **2011**, *4*, 1566–1569.

[43] Qian, L.; Gu, L.; Yang, L.; Yuan, H. Y.; Xiao, D. Direct growth of $NiCo_2O_4$ nanostructures on conductive substrates with enhanced electrocatalytic activity and stability for methanol oxidation. *Nanoscale* **2013**, *5*, 7388–7396.

[44] Heli, H.; Pishahang, J. Cobalt oxide nanoparticles anchored to multiwalled carbon nanotubes: Synthesis and application for enhanced electrocatalytic reaction and highly sensitive nonenzymatic detection of hydrogen peroxide. *Electrochim. Acta* **2014**, *123*, 518–526.

[45] Kong, L. J.; Ren, Z. Y.; Zheng, N. N.; Du, S. C.; Wu, J.; Tang, J. L.; Fu, H. G. Interconnected 1D Co_3O_4 nanowires on reduced graphene oxide for enzymeless H_2O_2 detection. *Nano Res.* **2015**, *8*, 469–480.

[46] Lei, X. M.; Li, T. T.; Zuo, Y. P.; Yin, W. M.; Wu, L.; Shao, K.; Xiao, X. Y.; Lu, Z. C.; Han, H. Y. Platinum-based nitrogen-doped porous C_xN_{1-x} compounds used as a transducer for sensitive detection of hydrogen peroxide. *Electrochim. Acta* **2016**, *209*, 661–670.

[47] Yan, Y. B.; Li, K. X.; Dai, Y. H.; Chen, X. P.; Zhao, J.; Yang, Y. H.; Lee, J.-M. Synthesis of 3D mesoporous samarium oxide hydrangea microspheres for enzyme-free sensor of hydrogen peroxide. *Electrochim. Acta* **2016**, *208*, 231–237.

[48] Ensafi, A. A.; Rezaloo, F.; Rezaei, B. Electrochemical sensor based on porous silicon/silver nanocomposite for the determination of hydrogen peroxide. *Sens. Actuators B: Chem.* **2016**, *231*, 239–244.

[49] Tang, K. K.; Wu, X. F.; Wang, G. D.; Li, L. X.; Wu, S. Y.; Dong, X. T.; Liu, Z. L.; Zhao, B. One-step preparation of silver nanoparticle embedded amorphous carbon for nonenzymatic hydrogen peroxide sensing. *Electrochem. Commun.* **2016**, *68*, 90–94.

[50] Huang, S.; Si, Z. C.; Li, X. K.; Zou, J. S.; Yao, Y. W.; Weng, D. A novel Au/r-GO/TNTs electrode for H_2O_2, O_2 and nitrite detection. *Sens. Actuators B: Chem.* **2016**, *234*, 264–272.

[51] Du, S. C.; Ren, Z. Y.; Wu, J.; Xi, W.; Fu, H. G. Vertical α-FeOOH nanowires grown on the carbon fiber paper as a free-standing electrode for sensitive H_2O_2 detection. *Nano Res.* **2016**, *9*, 2260–2269.

[52] Ding, Y.; Wang, Y.; Su, L.; Bellagamba, M.; Zhang, H.; Lei, Y. Electrospun Co_3O_4 nanofibers for sensitive and selective glucose detection. *Biosens. Bioelectron.* **2010**, *26*, 542–548.

[53] Chen, Y.; Prasad, K. P.; Wang, X. W.; Pang, H. C.; Yan, R. Y.; Than, A.; Chan-Park, M. B.; Chen, P. Enzymeless multi-sugar fuel cells with high power output based on 3D graphene-Co_3O_4 hybrid electrodes. *Phys. Chem. Chem. Phys.* **2013**, *15*, 9170–9176.